

Composition analysis and transition energies of ultrathin Sn-rich GeSn quantum wells

Inga A. Fischer^{1,*}, Caterina J. Clausen,² Daniel Schwarz,² Peter Zaumseil,³ Giovanni Capellini,^{3,4} Michele Virgilio,⁵ Maria Cecilia da Silva Figueira⁶, Stefan Birner⁶, Sebastian Koelling,⁷ Paul M. Koenraad,⁷ Michael R. S. Huang,⁸ Christoph T. Koch⁸, Torsten Wendav,⁹ Kurt Busch,^{9,10} and Jörg Schulze²

¹*Experimentalphysik und Funktionale Materialien, Brandenburgische Technische Universität Cottbus-Senftenberg, Erich-Weinert-Strasse 1, D-03046 Cottbus, Germany*

²*Institut für Halbleitertechnik, Universität Stuttgart, Pfaffenwaldring 47, D-70569 Stuttgart, Germany*

³*IHP, Im Technologiepark 25, D-15236 Frankfurt (Oder), Germany*

⁴*Dipartimento di Scienze, Università di Roma Tre, Viale Guglielmo Marconi, 446, 00146 Roma, Italy*

⁵*Dipartimento di Fisica “E. Fermi,” Università di Pisa, Largo Pontecorvo 3, I-56127 Pisa, Italy*

⁶*nextnano GmbH, Lichtenbergstrasse 8, D-85748 Garching bei München, Germany*

⁷*Photonics and Semiconductor Nanophysics, Department of Applied Physics, Eindhoven University of Technology, NL-5600 MB Eindhoven, The Netherlands*

⁸*AG Strukturforschung/Elektronenmikroskopie, Humboldt-Universität zu Berlin, Newtonstrasse 15, D-12489 Berlin, Germany*

⁹*AG Theoretische Optik & Photonik, Humboldt-Universität zu Berlin, Newtonstrasse 15, D-12489 Berlin, Germany*

¹⁰*Max-Born-Institut, Max-Born-Strasse 2A, D-12489 Berlin, Germany*



(Received 5 September 2019; revised manuscript received 19 December 2019; accepted 23 January 2020; published 19 February 2020)

While GeSn alloys with high Sn content constitute direct group-IV semiconductors, their growth on Si remains challenging. The deposition of a few monolayers of pure Sn on Ge and their overgrowth with Ge using molecular beam epitaxy can be a means of obtaining Sn-rich quantum wells with very high Sn content while maintaining high crystal quality. Here, we provide structural and compositional information on such structures with very high accuracy. Based on our characterization results we theoretically predict transition energies and compare them with experimental results from photoluminescence measurements. Our results constitute the groundwork for tuning the molecular beam epitaxy based growth of Sn-rich quantum wells and dots for applications in electronic and optoelectronic devices.

DOI: [10.1103/PhysRevMaterials.4.024601](https://doi.org/10.1103/PhysRevMaterials.4.024601)

I. INTRODUCTION

Alloying Ge with Sn is a path towards obtaining direct group-IV semiconductors and thus has become the subject of intense experimental efforts [1–4]. This is not only motivated by the aim of using a direct group-IV semiconductor material as the key towards better integration of optoelectronic functionality on chip but also by the potentially higher charge carrier mobilities that could be beneficial for the use of GeSn alloys in metal-oxide-semiconductor field-effect transistor (MOSFET) fabrication [5]. The alloy compositions required for obtaining the crossover of $\text{Ge}_{1-y}\text{Sn}_y$ from an indirect to a direct band gap material are predicted to vary between $y = 0.073$ for the relaxed alloy [6] and $y \approx 0.17$ [7] or $y \approx 0.19$ [6] for pseudomorphic $\text{Ge}_{1-y}\text{Sn}_y$ on Ge (001). However, the growth of bulk $\text{Ge}_{1-y}\text{Sn}_y$ alloys is highly challenging because of the low equilibrium solubility of Sn in Ge ($\sim 1\%$) [8] and the large lattice mismatch of 14.7% of the constituent elements. As a consequence, the growth of partially relaxed high-quality bulk $\text{Ge}_{1-y}\text{Sn}_y$ alloys with high Sn content often requires the use of Ge buffer layers with thicknesses $\geq 1 \mu\text{m}$ on Si wafers.

The fabrication of low-dimensional structures such as Sn-rich quantum wells or quantum islands could be a route towards the realization of $\text{Ge}_{1-y}\text{Sn}_y$ structures with a Sn content high enough to obtain a direct band gap material while at the same time mitigating the influence of the lattice constant mismatch on layer quality [9,10]. Additionally, carrier confinement in these low-dimensional structures can be utilized to improve optoelectronic device properties [11]. Finally, ultrathin films of Sn on Ge (111) have also been proposed as topological insulators [12]. All of these potential applications require a better understanding of the growth of ultrathin Sn films as well as intermixing effects with substrate and cap layers.

$\text{Ge}_{1-y}\text{Sn}_y$ quantum well structures with a width of several nanometers and $y \leq 0.125$ have been fabricated using both molecular beam epitaxy (MBE) [13–15] and chemical vapor deposition (CVD) methods [16]. A different route towards the growth of Sn-rich quantum well structures consisting of the deposition of a few monolayers (MLs) of pure Sn on Ge and overgrowth with Ge has been explored using MBE [17–21]. In early studies, the main objective using this approach was to fabricate superlattices containing, e.g., 20 periods consisting of 1 ML of Sn followed by either 11, 15, or 21 MLs of Ge [18]. Experimental investigations of optical properties of these structures showed no indication of carrier confinement, and the results were consistent with

*Corresponding author: inga.fischer@b-tu.de

theoretical predictions of an effective band structure using the virtual crystal approximation [20]. Subsequent growth experiments were based on the deposition of 2 MLs of Sn and their overgrowth with 5 and 10 nm of Ge [21] with the aim of creating Sn-rich quantum well (QW) and multiple quantum well (MQW) structures rather than superlattice structures. The Sn thickness was kept close to the critical layer thickness for the onset of 3D island growth, determined to be 2.25 MLs at a substrate temperature of 100 °C. In all of these growth experiments, Sn segregation across Sn/Ge heterointerfaces can be expected to cause unintended alloying and thus, heavily influence shape and composition of the low-dimensional, Sn-rich nanostructures [18,22].

Here, we investigate the deposition of pure Sn on Ge and overgrowth with Ge in detail. We determine the position-dependent Sn concentration in our Sn-rich MQW structures with subnanometer precision using atom probe tomography (APT) to obtain information on Sn segregation and diffusion in our Sn-rich wells [23,24]. Based on this structural information we theoretically predict transition energies in our structures and compare these predictions to low-temperature photoluminescence (PL) measurements on samples with a few Sn-rich wells. Our study thus constitutes an important step towards the realization of ultrathin Sn-rich layers with high layer quality and well-defined interfaces.

II. EXPERIMENT

For all samples, MBE was used for material deposition on Si (100) wafers of 100 mm diameter using an electron beam evaporator for Si and Knudsen cells for Ge and Sn with pyrolytic BN crucibles and with a base pressure below 10^{-10} mbar. Substrates were heated with a graphite resistor and the source fluxes were controlled with a feedback loop. The Si and Ge sources were calibrated to obtain fluxes of 1 \AA/s , while a lower growth rate of $<0.1 \text{ \AA/s}$ was used for Sn deposition. The Sn flux was calibrated using thin epitaxial $\text{Ge}_{1-y}\text{Sn}_y$ films and determining the Sn concentration by Rutherford backscattering spectroscopy (RBS). Prior to film deposition, all substrates were heated inside the MBE chamber to 900 °C for 5 min in order to remove the native SiO_2 surface layer by thermal desorption. First, a 50-nm Si buffer layer was deposited at 500 °C to cover surface contaminants and to provide a smooth surface. This was followed by the deposition of a Ge buffer layer grown at 1 \AA/s and 330 °C in two steps: After the growth of the first 50 nm of epitaxial Ge, an annealing step was carried out at 850 °C to reduce the threading dislocation density and form a virtual substrate. A second layer of Ge with a thickness of 150 nm was deposited to provide a smooth surface for the subsequent growth of high-quality layers.

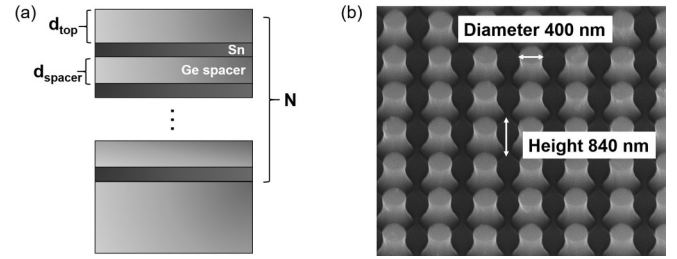


FIG. 1. (a) Schematic cross section of the samples. (b) Scanning electron microscope image of semiconductor nanopillars that were fabricated from the samples.

Three sample series were investigated; an overview of the relevant parameters is given in Fig. 1(a) and Table I. For the first series containing two samples, $N = 10$ layer stacks were grown at a substrate temperature of 100 °C by repeatedly depositing 2 MLs of Sn and covering the material with Ge spacer layers also deposited at a growth temperature of 100 °C. The spacer layer thicknesses d_{spacer} were set to 5 and 10 nm for the two samples. The Sn layer thickness was fixed at 2 MLs. This thickness is slightly below the critical Sn layer thickness of 2.25 MLs for the onset of 3D growth, which had previously been determined by atomic force microscopy (AFM) measurements on a series of samples onto which Sn layers of different thicknesses had been deposited [21]. First experimental results on the structural characterization of the samples of the first sample series, including transmission electron microscopy (TEM) analysis, were reported in Ref. [21]. Here, we used these samples to determine composition profiles and Sn segregation based on APT measurements. In the second sample series, the Sn layer thickness remained unchanged within experimental accuracy; the Ge spacer layer thickness was fixed at 10 nm but the number N of Sn-rich layers was reduced to 1, 3, and 5 layers.

The third sample series is identical to the second sample series except for the thickness d_{top} of the topmost layer, which was increased to 200 nm to facilitate patterning of the sample. These samples were structured into nanocolumns, with a diameter of 400 nm each and a lattice pitch of 1000 nm, using photolithography and reactive ion etching [Fig. 1(b)]. The columns were subsequently covered with 20 nm of Al_2O_3 using atomic layer deposition (ALD). Low-temperature PL measurements were performed, and the results were compared to theoretical predictions based on the position-dependent Sn content obtained from APT.

For sample characterization, transmission electron microscopy (TEM) using a JEM 2200 (JEOL Inc.) equipped with an energy-dispersive x-ray (EDX) detector was used to obtain information on the Sn-rich wells of sample series 2. Furthermore, APT using a LEAP 4000X HR from Cameca was used

TABLE I. Sample series and parameter variations (where N is the number of Sn-rich layers within the sample).

	Sample 1.1	Sample 1.2	Sample 2.1	Sample 2.2	Sample 2.3	Sample 3.1	Sample 3.2	Sample 3.3
d_{spacer} (nm)	5	10	10	10	10	10	10	10
d_{top} (nm)	5	10	10	10	10	200	200	200
N	10	10	1	3	5	1	3	5

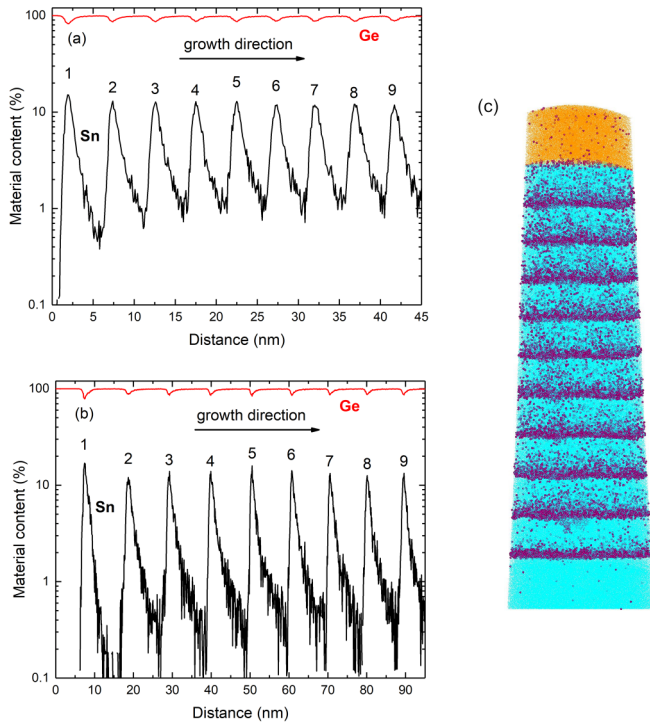


FIG. 2. (a) Position-dependent Sn and Ge content in the direction normal to the sample surface as obtained from APT for sample 1.1 and (b) sample 1.2. Peaks are numbered from 1 (first Sn-rich well in order of growth) to 9 (last Sn-rich well to be grown and closest to the sample surface). The origin on the distance axis is arbitrarily chosen to lie below the first Sn-rich well. The asymmetry of the Sn peak profiles is a consequence of Sn segregation during growth. We note that the data appear more noisy than in (a) as a result of the lower minimum Sn content. (c) Three-dimensional reconstructed image of the APT data for sample 1.2. The positions of 100% of detected Ge atoms are shown as light blue dots and 100% of detected Sn atoms are shown as violet spheres.

to extract the position-dependent Sn content of sample series 1. During APT, the samples were kept at a base temperature of 20 K and field evaporation was induced by picosecond laser pulses at a wavelength of 355 nm with a pulse energy of 5–10 pJ. The tips for APT were prepared in a FEI Nova Nanolab 600i using a previously published procedure [25] and a 5-kV cleaning step to minimize the damage induced in the sample. For additional structural characterization, x-ray diffraction (XRD) measurements were carried out with a SmartLab diffractometer from Rigaku using Cu $K\alpha$ radiation in order to obtain information on lattice constants and strain. Lastly, μ PL measurements were carried out using a custom-designed Horiba setup featuring a 50 \times optical microscope (numerical aperture NA = 0.65) and a laser with a 532-nm excitation wavelength, a high-resolution spectrometer optimized for NIR measurements (Horiba iHR320), and a single channel PbS detector (2.8- μ m cutoff wavelength detection range) connected to a lock-in amplifier. All spectra were collected at normal incidence in backscattering geometry using a 50 \times objective (NA = 0.65). A white-body lamp was used to determine the optical response of the setup used for the calibration. The low-temperature PL measurements were used to extract information on transition energies.

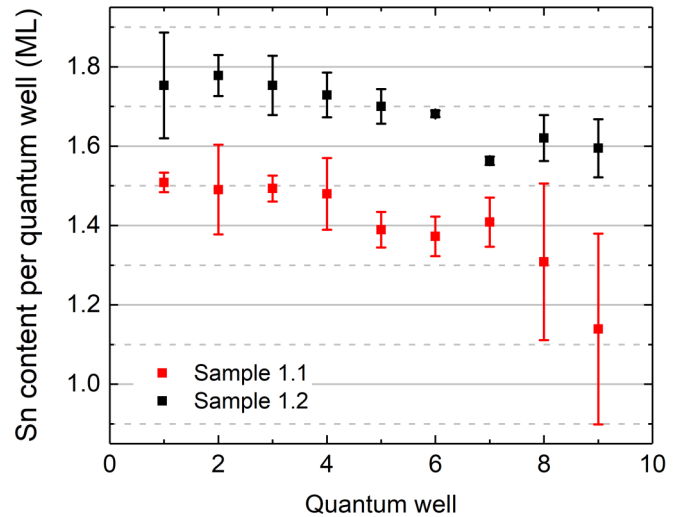


FIG. 3. Integrated Sn content per quantum well as extracted from the APT measurement data from two different tips per sample. The integrated amount of Sn per well can be seen to decrease with the number of wells as further indication of Sn segregation during sample growth.

III. RESULTS AND DISCUSSION

APT was performed on the samples of series 1, containing 10 layers of Sn-rich wells, in order to investigate how the variation in spacer layer thickness affects the Sn distribution within the sample and to obtain information on the position-dependent Sn content as input for the theoretical prediction of transition energies. Qualitatively, it can be seen that Sn segregation during growth results in a Sn profile that is smeared out along the growth direction for the two samples 1.1 and 1.2 (Fig. 2): For sample 1.1 with a Ge spacer thickness of 5 nm, the minimum Sn content between wells remains at \sim 1%, indicating that Sn segregation during growth leads to a poor separation between wells.

A more detailed analysis confirms this assumption: The integrated amount of Sn that is present in each well shows a gradual decline as the number of quantum wells increases (Fig. 3). While this is true for both sample 1.1 and sample 1.2, the decrease is more pronounced for sample 1.1, indicating a gradual accumulation of Sn on the sample surface. In the samples of the subsequent sample series, the thickness of the Ge spacer layer separating adjacent wells was, therefore, set to 10 nm.

In order to obtain more quantitative information, we performed a detailed analysis on the APT result for sample 1.2. The position-dependent Sn concentration is well represented by an exponentially modified Gaussian, i.e., the convolution of a Gaussian peak with an exponential function [26]. This functional form describes a diffusion-broadened profile with an exponential leading edge as a result of Sn segregation in the direction of growth during layer deposition. The following fit function is used for the peaks:

$$f(x) = y_0 + \frac{Aw}{t_0} \sqrt{\frac{\pi}{2}} \exp\left[\frac{1}{2} \left(\frac{w}{t_0}\right)^2 - \frac{x - x_c}{t_0}\right] \times \left[1 - \operatorname{erf}\left(\frac{w}{\sqrt{2}t_0} - \frac{x - x_c}{\sqrt{2}w}\right)\right]. \quad (1)$$

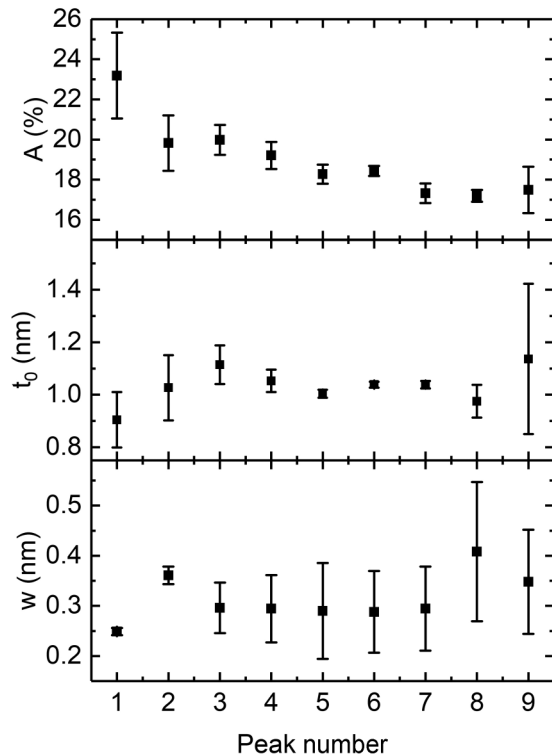


FIG. 4. Fit parameters for nine of the ten peaks corresponding to Sn-rich quantum wells obtained from two different APT measurements performed on sample 1.2.

Here, A is the amplitude, x_c the position, and w the width of the deconvoluted Gaussian peak; t_0 is the $1/e$ decay length. The parameter t_0 corresponds to the segregation length of Sn in Ge. Sample peak fits are shown in the Supplemental Material [27].

Fits were performed for nine of the ten peaks corresponding to Sn-rich wells, whereas the parameters for the topmost well could not be extracted with sufficient accuracy.

The resulting fit parameters are shown in Fig. 4. While the parameters extracted for peaks 2–9 are remarkably similar, the Sn content extracted from peak 1 is significantly higher. We attribute this effect to sample heating as a result of the opening of the shutter of the Sn effusion cell, which causes the Sn wells numbered 2–10 to be grown at an effectively higher substrate temperature. From fits to peaks 2–9 we extract a Sn segregation length of 1.04 ± 0.14 nm. Furthermore, we find that even at growth temperatures as low as 100 °C, a small amount of Ge and Sn interdiffusion at the layer-substrate interface results in a finite width of the deconvoluted Gaussian peak. This can be expected to have consequences, e.g., for the deposition of pure Sn layers on Ge (111) with the aim of observing quantum spin Hall states. Finally, there is a downwards trend in the amplitude of the Sn peak with increasing peak number, which mirrors the trend observed in the number of Sn monolayers in each well; see Fig. 3.

APT can be used to obtain information on position-dependent composition with very high accuracy. However, the method is time consuming. XRD analysis is a faster and nondestructive method for structural analysis, which yields complementary information. Here, we compare the information we infer from XRD analysis with data obtained from APT. Since the previous analysis showed that, with an interwell spacing of only 5 nm, individual wells cannot be reliably separated, we restrict ourselves to samples 1.2, 2.1, 2.2, and 2.3 with an interwell spacing of 10 nm. Reciprocal space maps (RSMs) of those samples confirm that all samples show pseudomorphic growth on Ge (Fig. 5).

Since the amount of Sn deposited for each well is low and, therefore, highly sensitive to growth variations, we verified the reproducibility of growth for our sample series by comparing samples 1.2 and 2.3 as follows: The average MQW periodicity d was obtained from ω - 2θ scans and the unstrained lattice constant a_0 of the MQW structures was extracted from the RSM, approximating the elastic constants by their values for pure Ge [28]. The average Sn content per MQW period of $d \sim 10$ nm was obtained from a linear interpolation of the

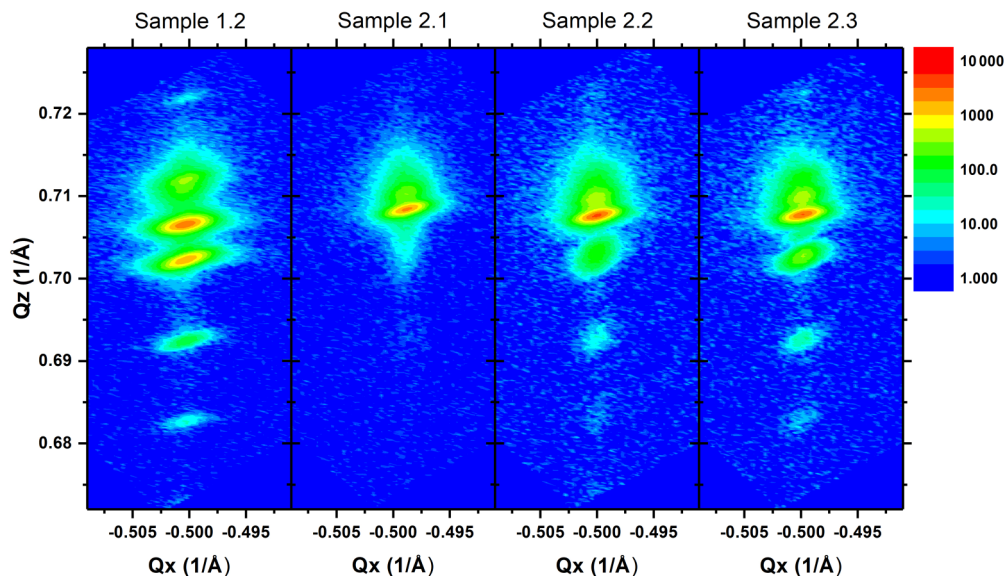


FIG. 5. RSM around the $(-2 -2 4)$ Bragg reflection for all unstructured samples with a Ge spacer thickness of 10 nm.

TABLE II. Periodicity of the MQW structure and average Sn content per well extracted from XRD measurements.

	a_0 (nm)	d (nm)	Average Sn content per MQW period	Calculated amount of Sn deposited (ML)
Sample 1.2	0.5678	10.16	0.0243	1.75
Sample 2.3	0.5678	10.11	0.0242	1.73

lattice constants of Ge (0.565 79 nm) and Sn (0.6493 nm) and used to calculate the thickness of the deposited Sn layer in monolayers (Table II).

In both cases, the calculated amount of Sn deposited for each QW is close to but below the intended 2 MLs. The remaining difference can be a result of Sn segregation. The difference between the two samples is less than 2%.

TEM images of samples 2.1, 2.2, and 2.3 confirm the existence of Sn-rich wells in the samples of series 2 (Fig. 6). While the EDX scan results show asymmetric Sn profiles (see Supplemental Material [27]), the positional accuracy remains below that of APT and is not used to directly extract the QW profiles.

The position-dependent material composition obtained from APT measurements (Fig. 2) is the starting point for band structure calculations in order to predict transition energies in our structures and compare with PL measurements. While XRD data show (Fig. 5) that all samples were grown pseudomorphically on Ge, it has been shown previously that strain can be altered postgrowth by structuring the material [29–31] and/or employing silicon nitride stressor layers [32]. In particular, partial or complete material relaxation was achieved in III-V MQW structures by structuring the samples into micropillars [29,30]. Here, we therefore discuss theoretical results for the position-dependent band profiles as well as energy levels of Sn-rich wells, assuming both strained (corresponding to pseudomorphic growth on Ge) and relaxed Sn-rich wells. All calculations were performed using the NEXTNANO simulation software [33]. In order to enable comparison with PL measurements on samples with one, three, or five Sn-rich quantum wells (see Table I), the compositional profile for the semiconductor layers was represented by peak 1 from the APT analysis [Fig. 2(b)] for one Sn-rich quantum well, peaks 1–3 for three Sn-rich quantum wells, and by peaks 1–5 for five Sn-rich quantum wells. All model parameters, except for the band gaps, were approximated by linear interpolations of the model parameters for Ge and Sn. Quadratic interpolation was used to calculate the band gap

energies,

$$E_{g,\zeta}(\text{Ge}_{1-y}\text{Sn}_y) = (1-y)E_{g,\zeta}(\text{Ge}) + yE_{g,\zeta}(\text{Sn}) - b_{g,\zeta}^{\text{GeSn}}y(1-y).$$

Here, $b_{g,\zeta}^{\text{GeSn}}$ are the bowing parameters and $\zeta = \Gamma, L$ refers to the different conduction band valleys. The temperature dependence of the band gap energies is taken into account using Varshni's relation [34],

$$E_{g,\zeta}(T) = E_{g,\zeta}^0 - \alpha_\zeta \frac{T^2}{T + \beta_\zeta}.$$

An overview of the material parameters used in calculations is given in Table S2 in the Supplemental Material [27]. While the material parameters for Ge that can be found in the literature are rather well known, the choice of material parameters used for α -Sn, in particular the band offsets and temperature-dependent band gaps, requires a more detailed justification.

A thorough discussion of the direct band gap of $\text{Ge}_{1-y}\text{Sn}_y$ and experimentally determined bowing parameters can be found, e.g., in Ref. [6] and will not be repeated here. We simply note that the value of the direct band gap of α -Sn used in our calculations was determined experimentally from interband magnetoreflexion measurements and found to be independent of temperature for temperatures between 1.5 and 85 K [35]. We therefore set the Varshni parameters for the direct band gap of α -Sn to zero. Following Ref. [36] we chose the bowing parameter of the band gap at the Γ point as $b_{g,\Gamma}^{\text{GeSn}} = 2.42$ eV for our calculations.

Experimental values for the indirect band gap $E_{g,L}$ of α -Sn vary. Lavine and Ewald [37] extracted $E_{g,L} = 0.092$ eV from transport data obtained at $T = 4.2$ K and found a temperature dependence $E_{g,L}(T) = E_{g,L}^0 - \gamma T$, with $\gamma = 0.04$ meV/K, for measurements between $T = 100$ K and $T = 170$ K. An analysis by Broerman [38] carried out on the measured reflectivity at the plasma edge of α -Sn obtained by Wagner and Ewald [39] yielded $E_{g,L}^0 = 0.110$ eV and $\gamma = 0.4$ meV/K. A magnetotransport and magneto-optical study of α -Sn grown on CdTe substrates by MBE found $E_{g,L}(300\text{ K}) = 0.007$ eV [40], which was corrected to 0.006 eV after taking strain into account [6], with $\gamma = 0.36$ meV/K. Here, we chose to set $E_{g,L}^0 = 0.093$ eV, $\alpha_L = 0.29$ meV/K, and $\beta_L = 0$ K in order to linearly interpolate between the experimental values $E_{g,L}(4.2\text{ K}) = 0.092$ eV and $E_{g,L}(300\text{ K}) = 0.006$ eV. Compared to experimental results, theoretical predictions for $E_{g,L}^0$ seem to overestimate its value, with $E_{g,L}^0 = 0.140$ eV obtained from nonlocal pseudopotential calculations [41] and $E_{g,L}^0 = 0.175$ eV obtained from local-density approximation [42].

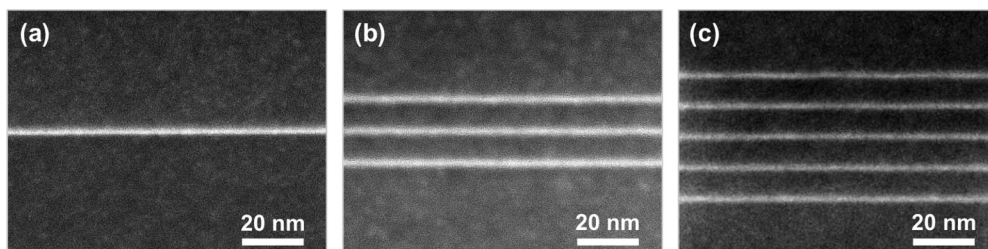


FIG. 6. Cross-sectional high-angle annular dark-field (HAADF) images of samples (a) 2.1, (b) 2.2, and (c) 2.3.

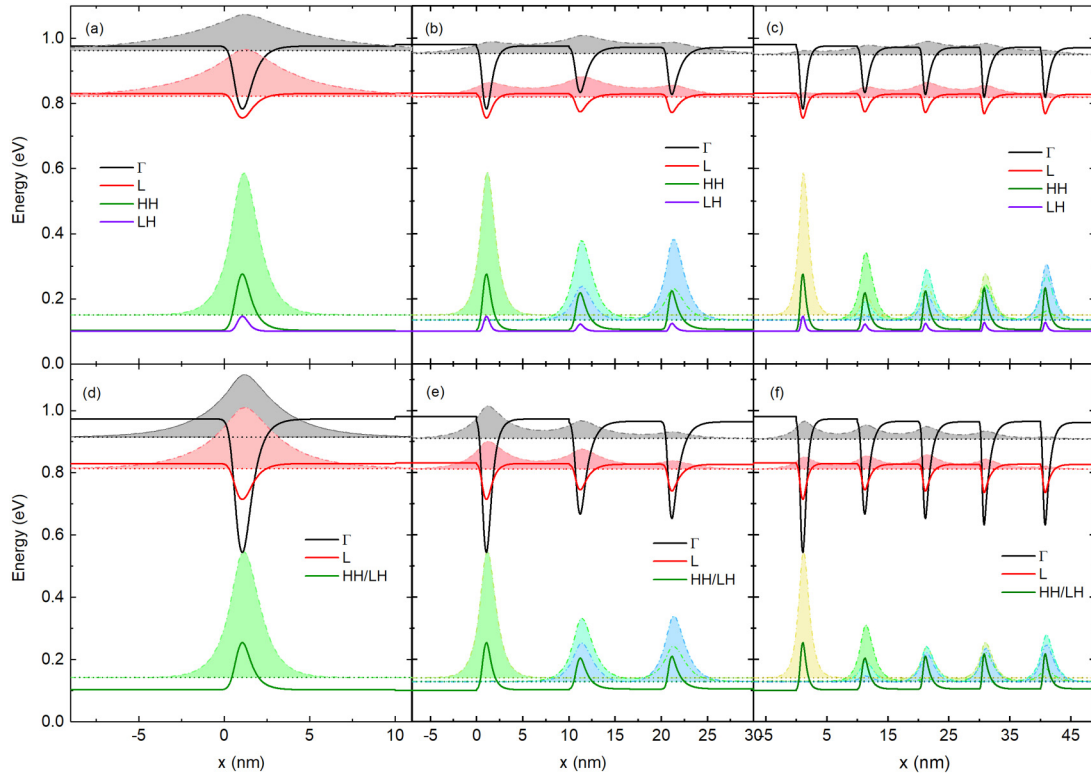


FIG. 7. Calculations of the position-dependent potential profiles, energy levels, and near-gap subband states at $T = 80$ K and with a valence band offset (VBO) of 0.69 eV for 1, 3, and 5 Sn-rich quantum wells assuming pseudomorphic growth on Ge (i.e., including strain) (a)–(c) and full relaxation (i.e., without strain) (d)–(f). The positions of the lowest energy levels are shown as dashed lines.

The compositional dependence of the indirect band gap $E_{g,L}$ of the alloy $\text{Ge}_{1-y}\text{Sn}_y$ has been studied experimentally by low-temperature ($T = 10$ K) PL measurements on MBE-grown $\text{Ge}_{1-y}\text{Sn}_y$ quantum well structures [7,43] and by room-temperature PL measurements on bulk $\text{Ge}_{1-y}\text{Sn}_y$ samples grown by CVD [6]. Tonkikh *et al.* [7] report a value $b_{g,L}^{\text{GeSn}} = 0.80$ eV for the bowing parameter; subsequent PL experiments on MBE-grown $\text{Ge}_{1-y}\text{Sn}_y$ quantum well structures by the same group yielded $b_{g,L}^{\text{GeSn}} = 1.47$ eV [43]. Here, we use the more recent value $b_{g,L}^{\text{GeSn}} = 1.03$ eV obtained in Ref. [6], which lies between the previously obtained values, and note that this choice is consistent with $E_{g,L}(300\text{ K}) = 0.006$ eV. A detailed comparison of the experimentally obtained values for $b_{g,L}^{\text{GeSn}}$ with predictions from theory can be found in Ref. [6].

Band offsets are often approximated according to Jaros's theory [44] in calculations of heterostructure properties involving $\text{Ge}_{1-y}\text{Sn}_y$ alloys [45,46]. Jaros's theory, which can be used to calculate the unstrained average valence band offsets between elemental semiconductors, predicts an offset $\Delta E_{v,\text{Jaros}} = 0.69$ eV between Ge and α -Sn, with the higher energy on the α -Sn side. Here, the averaging involves the heavy, light, and split-off hole bands. The average band offset at a $\text{Ge}_{1-y}\text{Sn}_y/\text{Ge}$ interface is obtained by interpolation, i.e., $\Delta E_{v,\text{Jaros}}(\text{Ge}_{1-y}\text{Sn}_y/\text{Ge}) = 0.69y$ eV. A later study by Li *et al.* [47] that explicitly takes the effect of lattice mismatch between the elemental semiconductors into account reports a higher average valence band offset of $\Delta E_{v,\text{Li}} = 1.02$ eV. In the absence of a detailed experimental investigation, it is *a priori* not clear which value should be assumed in the calculation and, therefore, this parameter will be varied.

For $\Delta E_{v,\text{Jaros}} = 0.69$ eV, our theoretical calculation reproduces a type-I quantum well structure both for pseudomorphic, i.e., strained, [Figs. 7(a)–7(c)] and for fully relaxed [Figs. 7(d)–7(f)] $\text{Ge}_{1-y}\text{Sn}_y$ layers. For all cases, the indirect transition is lowest in energy. Furthermore, the low effective masses of the electrons (see Sec. 3 of the Supplemental Material [27]) in conjunction with the very low thickness of the Sn-rich well lead to poor electron confinement and an electron wave function that is delocalized over all wells in the samples with three and five Sn-rich wells (Fig. 7). Concerning the holes, we find that only the first Sn-rich well in the growth direction has a compositional profile that leads to a hole wave function fully localized within the well. This leads to a reduced overlap of electron and hole wave functions as the number of Sn-rich wells is increased: The inner product between the electron and heavy hole wave functions corresponding to the lowest energy levels gets reduced from 0.8 to 0.27 as the number of wells is increased from 1 to 3, for example.

PL spectra thus can be expected to show contributions from band-to-band recombination accompanied by spontaneous emission of phonons, which provide the missing momentum for the indirect transition, as well as recombination processes, in which the momentum difference is supplied by elastic scattering channels. As such, the peak energies extracted from measurements can be expected to be lower than the calculated transition energies. To estimate this difference we assume a phonon energy $\text{TO}_{\text{Ge-Ge}} = 36$ meV of bulk Ge [48] and attribute an additional ~ 5 meV to the indirect exciton binding energy [7].

TABLE III. Calculated transition energies at 80 K for 1 Sn-rich well assuming different values for the valence band offset.

	Transition energy		
	$\Delta E_v = 0.69$ eV	$\Delta E_v = 1.02$ eV	$\Delta E_v = 1.35$ eV
1 Sn-rich well (strained, pseudomorphic)	0.671 eV	0.653 eV	0.627 eV
1 Sn-rich well (relaxed)	0.670 eV	0.657 eV	0.636 eV

In our samples, transition energies are potentially sensitive to variations in well thickness and material composition: locally, the material composition can deviate from the results obtained in APT analysis, leading to a reduction in transition energies observed in experiment. We have endeavored to quantify the influence of composition fluctuations on the simulation results as follows: We carried out calculations for the altogether four quantum well profiles resulting from fits to the first peaks of the APT data obtained for samples 1.1 and 1.2 (see Fig. 3). The fit results as well as the calculated transition energies can be found in the Supplemental Material [27]. The difference between the largest and smallest transition energy is 13 meV.

Remaining uncertainties in material parameters such as effective masses could also affect the accuracy of our calculations. However, when calculating transition energies for different assumed values of the effective masses reported in Table S2 [27], the resulting changes are small. While m_{HH} has the overall largest influence on calculated transition energies, changing, e.g., the material parameter $m_{l,L}(\text{Ge})$ from $1.610 m_0$ to $1.568 m_0$, while keeping all other parameters fixed, for example, leads to a change in transition energy of only 1 meV. Indeed, the effective charge carrier masses in combination with the low well thickness lead to energy levels within the conduction and valence band wells, which are close to the band edges of the surrounding Ge. This results in a weak influence of changes in the position-dependent potential profiles on the energies of the electron and hole levels. Perhaps the most striking demonstration of this fact is the observation that the introduction of strain, which strongly changes the conduction band potential well shape, leads to only a small shift in the calculated indirect transition energies: The calculated transition energies for strained (pseudomorphic) and fully relaxed Sn-rich wells differ by less than 10 meV (Table III).

We find that the parameter with the largest impact on the magnitude of the calculated transition energies is the valence band offset between Ge and Sn. In Table III, we present calculation results for transition energies assuming $\Delta E_v = 0.69$ eV, $\Delta E_v = 1.02$ eV, and $\Delta E_v = 1.35$ eV. For higher values of ΔE_v the quantum well profile changes from a type-I to a type-II configuration in the unstrained material (Fig. 8).

Finally, Varshni's formula predicts a decrease in transition energy with increasing lattice temperature (Table IV).

In order to obtain experimental information on transition energies and compare the results to theoretical predictions, μPL measurements were performed on the samples of series

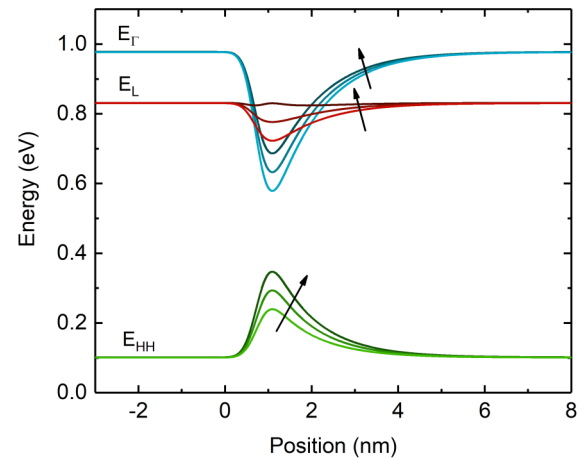


FIG. 8. Calculated well profiles for sample 3.1 at $T = 80$ K and for three different choices of the VBO $\Delta E_v = 0.69$, 1.02, and 1.35 eV (the arrows indicate an increase in VBO assumed in calculation).

2 and series 3. The signal intensity obtained from the samples of series 2 in the μPL measurement setup was too weak to allow for peak extraction. While we included PL data for series 2 obtained from a different measurement setup in the Supplemental Material [27], we restrict the following results and discussion to data obtained from series 3. An increase in PL signal intensity in structured nanocolumn samples compared to the unstructured samples has been observed previously [49] and was attributed to an increase in absorption of the incident light due to the antireflective properties of the patterned surface as well as an increase in the effective penetration depth of the incident laser light.

The power-dependent and temperature-dependent spectra of samples 3.1, 3.2, and 3.3 are shown in Fig. 9. It is immediately apparent that the PL intensity is reduced as the number of Sn-rich GeSn QWs increases. One possible reason for this is poor electron confinement in the conduction band wells as obtained from theoretical calculations (Fig. 7), which leads to a decrease in wave function overlap. Another possible explanation could be an increase in point defects as the number of wells is increased, which can lead to a decrease in radiative recombination efficiency.

In the following, we restrict our experimental analysis to the samples with only one Sn-rich QW, i.e., sample 3.1. In order to extract information on peak energies and areas, Gaussian peak fits were performed on the data.

We expect a power-law dependence of the integrated intensity I on the excitation power P , i.e., $I \propto P^\alpha$ (Fig. 10). Here, with $\alpha = 1.79$, we observe a superlinear dependence of the integrated PL intensity on excitation power at low excitation powers, indicating that nonradiative recombination channels in the form of trap states are present in the samples.

TABLE IV. Calculated transition energies for sample 3.1 at various lattice temperatures. A VBO of 1.35 eV was chosen.

80 K	90 K	110 K	140 K	180 K	230 K
0.636 eV	0.633 eV	0.628 eV	0.6202 eV	0.608 eV	0.591 eV

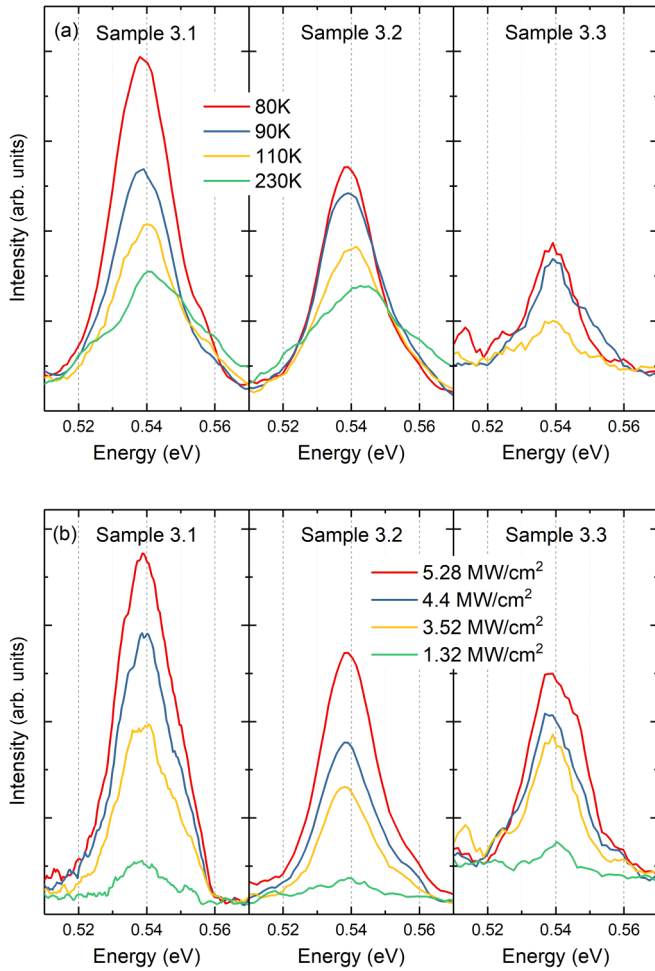


FIG. 9. (a) Temperature-dependent μ PL spectra of samples 3.1 (one Sn-rich QW) to 3.3 (five Sn-rich QWs) at a constant excitation power density of 5.28 MW/cm². (b) Selected power-dependent μ PL spectra of samples 3.1 (one Sn-rich QW) to 3.3 (five Sn-rich QWs) at a constant lattice temperature of 80 K.

In our sample, remaining threading dislocations that were not eliminated during the formation of the Ge virtual substrate on Si and point defects as a result of the sample growth process can be expected as the origin of the trap states. Those saturate with increasing excitation power, leading to a dependence of I on P that is still superlinear but with a lower value $\alpha = 1.33$ for the exponent.

When comparing the power-dependent spectra, the dependence of peak position on the excitation power can be seen to be weak [Fig. 11(a)]. This is indicative of a type-I quantum well structure.

Prior to comparing the theoretically predicted transition energies with results extracted from PL measurements, we will briefly discuss the role of strain in this comparison. Based on previous investigations involving III-V MQW nanopillar samples with nanopillar diameters up to 900 nm we can expect at least partial relaxation of the Sn-rich quantum wells in the circumference of the nanocolumns in our structured samples [29,31]. This strain relaxation is often detected via shifts in PL peak positions [29]. In our case, however, theoretical calculations predict less than 10 meV difference

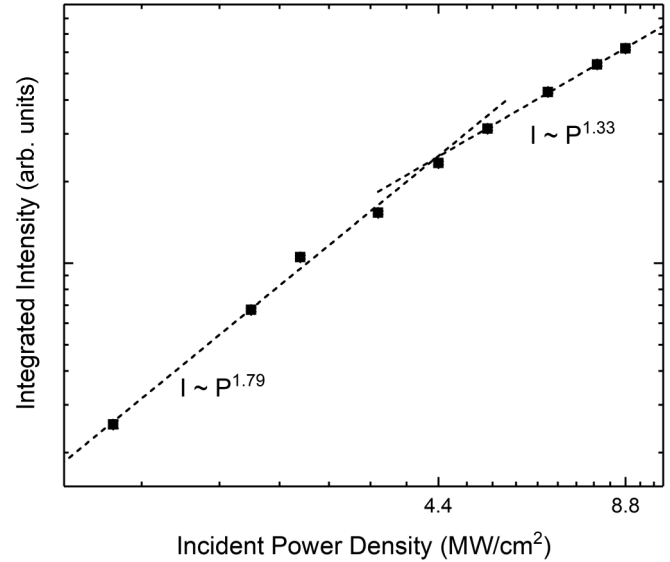


FIG. 10. Integrated intensity as a function of excitation power for sample 3.1 (one Sn-rich well) at a constant lattice temperature of 80 K.

in peak positions for fully relaxed samples compared to pseudomorphically strained ones (Table III). As a result, we cannot expect to extract information on the strain state of the nanocolumns from PL measurements. On the other hand, this enables us to compare experimentally determined PL peak positions to theoretical predictions for transition energies even without fully knowing the position-dependent strain in our nanocolumns.

Theoretical calculations showed that the band offset is the parameter with the largest influence on transition energies. Using $\Delta E_v = 0.69$ eV obtained from Jaros’s theory leads to a calculated transition energy of 0.670 eV for sample 3.1. If we assign the peaks observed in PL measurements to transitions involving heavy holes and electrons in the L valley of the conduction band, i.e., indirect transitions, our theoretical predictions exceed the measurement result of 0.539 eV by ~ 100 meV when phonon and exciton energies are taken into account. Increasing ΔE_v to 1.35 eV reduces this difference

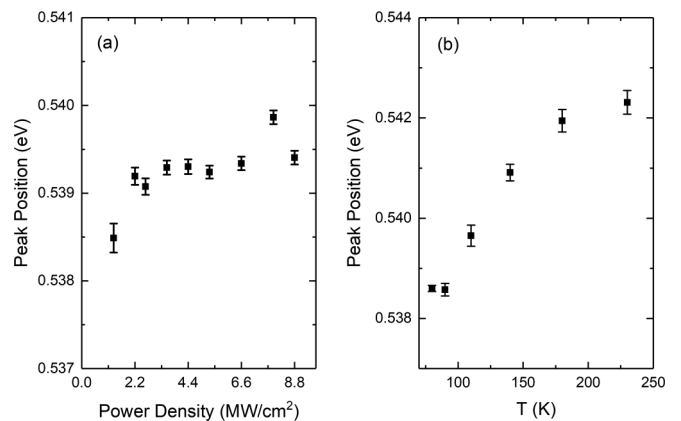


FIG. 11. (a) Dependence of peak position on excitation power at a constant lattice temperature of 80 K for sample 3.1 (one Sn-rich well). (b) Dependence of peak position on temperature at a constant excitation power density of 5.28 MW/cm² for sample 3.1.

to ~ 50 meV. We thus find that a considerably larger valence band offset than the one obtained from Jaros's theory has to be assumed in our calculations in order to reduce the discrepancy between experimentally obtained and simulated transition energies to the point where the remaining disagreement is $\sim 10\%$ of the experimental value. This also supports our assumption that the PL signal originates from indirect transitions since the direct transition energies are predicted to be considerably larger (Fig. 7). Finally, the comparatively low intensity of the PL signal also points towards indirect transitions as the origin of light emission.

We attribute the remaining difference of 50 meV in experimentally measured and theoretically predicted transition energies mainly to parameter uncertainties as well as uncertainties in the quantum well profile. We cannot rule out local fluctuations in thickness of the Sn-rich wells, which can result in changes in the band profile and reduced transition energies. Another contributing factor could be local heating induced by the incident laser, which can lead to uncertainties in the temperature-dependent band gap energies. Most importantly, since the influence of all material parameters on transition energies is small compared to the influence of the valence band offset, our results suggest that an accurate experimental determination of the valence band offset should be attempted in order to improve the predictive power of Ge/GeSn heterostructure calculations.

Finally, while Varshni's formula predicts a decrease in transition energy with increasing lattice temperature (Table IV), we observe a slight increase (4 meV as the lattice temperature is increased from 80 to 230 K) in transition energy in experiment [Fig. 11(b)]: Charge carriers can occupy higher energy levels as the lattice temperature is increased, leading to a net blueshift in energy levels.

IV. CONCLUSION

The MBE-based deposition of 2 MLs of Sn and their overgrowth with Ge at low substrate temperatures of 100°C leads to well-defined quantum wells with a peak Sn content of $\sim 15\%$. APT measurements reveal that the Sn peaks are asymmetric in the growth direction as a result of Sn segregation during layer deposition, while Sn diffusion leads to additional broadening of the Sn distribution profile.

For our structures, we were able to determine the segregation length $t_0 = 1.04 \pm 0.14$ nm of pure Sn deposited on Ge and overgrown with Ge with very high accuracy. One possible strategy to mitigate Sn segregation and Sn diffusion consists of depositing a few monolayers of Si.

Guo *et al.* have previously utilized ultrathin Si layers for metal-oxide-semiconductor field-effect transistor (MOSFET) channel passivation with reduced Sn segregation [50]. Here, a few monolayers of Si could also be used to reduce Sn segregation when deposited directly on top of the Sn layers prior to Ge overgrowth. Investigating the effect of Si on the suppression of Sn segregation and diffusion is also important when considering the growth of a few monolayers of Sn as topological insulators.

Theoretical predictions of transition energies indicate that radiative recombination is dominated by indirect transitions: While the peak amount of Sn in the wells is high, the small width of the well and the low electron masses along the confinement direction lead to a large separation of the energy levels in the Γ and the L bands so that indirect transitions remain favorable. When comparing our theoretical predictions to PL measurement results our band structure calculations overestimate the transition energies by 50 meV, provided that the valence band offset is chosen appropriately. We find that the valence band offset is the parameter with the largest influence on the values of the simulated transition energies. In order to improve agreement between experiment and simulation to within 10% of each other we had to increase the valence band offset significantly from the value predicted by Jaros [44], which is often used in simulations of Ge/GeSn heterostructures. Our results thus prompt us to call for a more detailed experimental investigation of the valence band offset between Ge and GeSn.

The effective masses of electrons in GeSn alloys with high Sn content in the Γ and L valleys impose limits on the well width when the binary alloy is used in (multiple-) quantum well structures designed to exhibit direct band gap optical transitions. In our growth strategy, the amount of Sn deposited cannot be increased without incurring 3D island growth. The growth of superlattices, in which a few monolayers of Sn, Ge, (and Si) are deposited in succession, could be a means for growing quantum wells with high Sn content and, most importantly, well-defined heterointerfaces. Alternatively, the growth of Sn islands could be specifically targeted and their overgrowth with Ge could be explored in order to obtain an island height that is large enough for the direct transition to dominate.

ACKNOWLEDGMENT

The authors acknowledge the support from Deutsche Forschungsgemeinschaft under Grants No. FI 1511/4-1, No. BU 1107/11-1, No. CA 1474/3-1, and No. KO 2911/13-1.

-
- [1] J. Kouvetakis, J. Menendez, and A. V. G. Chizmeshya, *Annu. Rev. Mater. Res.* **36**, 497 (2006).
 - [2] Z. P. Zhang, Y. X. Song, Z. Y. S. Zhu, Y. Han, Q. M. Chen, Y. Y. Li, L. Y. Zhang, and S. M. Wang, *AIP Adv.* **7**, 045211 (2017).
 - [3] M. Oehme, K. Kosteci, M. Schmid, F. Oliveira, E. Kasper, and J. Schulze, *Thin Solid Films* **557**, 169 (2014).
 - [4] S. Wirths, R. Geiger, N. von den Driesch, G. Mussler, T. Stoica, S. Mantl, Z. Ikonik, M. Luysberg, S. Chiussi, J. M. Hartmann, H. Sigg, J. Faist, D. Buca, and D. Grützmacher, *Nat. Photonics* **9**, 88 (2015).
 - [5] X. Gong, G. Han, F. Bai, S. Su, P. Guo, Y. Yang, R. Cheng, D. Zhang, G. Zhang, C. Xue, B. Cheng, J. Pan, Z. Zhang, E. S. Tok, D. Antoniadis, and Y. C. Yeo, *IEEE Electron Device Lett.* **34**, 339 (2013).
 - [6] L. Jiang, J. D. Gallagher, C. L. Senaratne, T. Aoki, J. Mathews, J. Kouvetakis, and J. Menéndez, *Semicond. Sci. Technol.* **29**, 115028 (2014).
 - [7] A. A. Tonkikh, C. Eisenschmidt, V. G. Talalaev, N. D. Zakharov, J. Schilling, G. Schmidt, and P. Werner, *Appl. Phys. Lett.* **103**, 032106 (2013).

- [8] C. D. Thurmond, F. A. Trumbore, and M. Kowalchik, *J. Chem. Phys.* **25**, 799 (1956).
- [9] T. Wendav, I. A. Fischer, M. Virgilio, G. Capellini, F. Oliveira, M. F. Cerqueira, A. Benedetti, S. Chiussi, P. Zaumseil, B. Schwartz, K. Busch, and J. Schulze, *Phys. Rev. B* **94**, 245304 (2016).
- [10] F. Oliveira, I. A. Fischer, A. Benedetti, M. F. Cerqueira, M. I. Vasilevskiy, S. Stefanov, S. Chiussi, and J. Schulze, *J. Appl. Phys.* **117**, 125706 (2015).
- [11] K. L. Wang, D. Cha, J. Liu, and C. Chen, *Proc. IEEE* **95**, 1866 (2007).
- [12] Y. Fang, Z.-Q. Huang, C.-H. Hsu, X. Li, Y. Xu, Y. Zhou, S. Wu, F.-C. Chuang, and Z.-Z. Zhu, *Sci. Rep.* **5**, 14196 (2015).
- [13] G.-E. Chang, W.-Y. Hsieh, J.-Z. Chen, and H. H. Cheng, *Opt. Lett.* **38**, 3485 (2013).
- [14] J.-Z. Chen, H. Li, H. H. Cheng, and G.-E. Chang, *Opt. Mater. Express* **4**, 1178 (2014).
- [15] B. Schwartz, M. Oehme, K. KostECKI, D. Widmann, M. Gollhofer, R. Koerner, S. Bechler, I. A. Fischer, T. Wendav, E. Kasper, J. Schulze, and M. Kittler, *Opt. Lett.* **40**, 3209 (2015).
- [16] D. Stange, N. von den Driesch, D. Rainko, C. Schulte-Braucks, S. Wirths, G. Mussler, A. T. Tiedemann, T. Stoica, J. M. Hartmann, Z. Ikonik, S. Mantl, D. Grützmacher, and D. Buca, *Opt. Express* **24**, 1358 (2016).
- [17] W. Wegscheider, K. Eberl, U. Menczigar, and G. Abstreiter, *Appl. Phys. Lett.* **57**, 875 (1990).
- [18] W. Wegscheider, J. Olajos, U. Menczigar, W. Dondl, and G. Abstreiter, *J. Cryst. Growth* **123**, 75 (1992).
- [19] K. Eberl, W. Wegscheider, and G. Abstreiter, *J. Cryst. Growth* **111**, 882 (1991).
- [20] P. Vogl, J. Olajos, W. Wegscheider, and G. Abstreiter, *Surf. Sci.* **267**, 83 (1992).
- [21] F. Oliveira, I. A. Fischer, A. Benedetti, P. Zaumseil, M. F. Cerqueira, M. I. Vasilevskiy, S. Stefanov, S. Chiussi, and J. Schulze, *Appl. Phys. Lett.* **107**, 262102 (2015).
- [22] H. Li, C. Chang, T. P. Chen, H. H. Cheng, Z. W. Shi, and H. Chen, *Appl. Phys. Lett.* **105**, 151906 (2014).
- [23] A. Kumar, J. Demeulemeester, J. Bogdanowicz, J. Bran, D. Melkonyan, C. Fleischmann, F. Gencarelli, Y. Shimura, W. Wang, R. Loo, and W. Vandervorst, *J. Appl. Phys.* **118**, 025302 (2015).
- [24] S. Assali, A. Dijkstra, A. Li, S. Koelling, M. A. Verheijen, L. Gagliano, N. von den Driesch, D. Buca, P. M. Koenraad, J. E. M. Haverkort, and E. P. A. M. Bakkers, *Nano Lett.* **17**, 1538 (2017).
- [25] K. Thompson, D. Lawrence, D. J. Larson, J. D. Olson, T. F. Kelly, and B. Gorman, *Ultramicroscopy* **107**, 131 (2007).
- [26] J. P. Foley and J. G. Dorsey, *J. Chromatogr. Sci.* **22**, 40 (1984).
- [27] See Supplemental Material at <http://link.aps.org/supplemental/10.1103/PhysRevMaterials.4.024601> for additional structural and compositional information, calculated transition energies for different extracted profile shapes, information on material parameters used in calculations, and photoluminescence data for sample series 2.
- [28] O. Madelung, M. Schultz, and H. Weiss, *Physics of Group IV Elements and III-V Compounds* (Springer-Verlag, New York, 1982).
- [29] P. Yu, C. H. Chiu, Y.-R. Wu, H. H. Yen, J. R. Chen, C. C. Kao, H.-W. Yang, H. C. Kuo, T. C. Lu, W. Y. Yeh, and S. C. Wang, *Appl. Phys. Lett.* **93**, 081110 (2008).
- [30] N. Thillosen, K. Sebald, H. Hardtdegen, R. Meijers, R. Calarco, S. Montanari, N. Kaluza, J. Gutowski, and H. Lüth, *Nano Lett.* **6**, 704 (2006).
- [31] Y. Ou, D. Iida, J. Liu, K. Wu, K. Ohkawa, A. Boisen, P. M. Petersen, and H. Ou, *Nanophotonics* **7**, 317 (2018).
- [32] R. W. Millar, D. C. S. Dumas, K. F. Gallacher, P. Jahandar, C. MacGregor, M. Myronov, and D. J. Paul, *Opt. Express* **25**, 25374 (2017).
- [33] A. Trellakis, T. Zibold, T. Andlauer, S. Birner, R. K. Smith, R. Morschl, and P. Vogl, *J. Comput. Electron.* **5**, 285 (2006).
- [34] Y. P. Varshni, *Physica* **34**, 149 (1967).
- [35] S. H. Groves, C. R. Pidgeon, A. W. Ewald, and R. J. Wagner, *J. Phys. Chem. Solids* **31**, 2031 (1970).
- [36] H. Lin, R. Chen, W. Lu, Y. Huo, T. I. Kamins, and J. S. Harris, *Appl. Phys. Lett.* **100**, 102109 (2012).
- [37] C. F. Lavine and A. W. Ewald, *J. Phys. Chem. Solids* **32**, 1121 (1971).
- [38] J. G. Broerman, *Phys. Rev. B* **5**, 397 (1972).
- [39] R. J. Wagner and A. W. Ewald, *J. Phys. Chem. Solids* **32**, 697 (1971).
- [40] C. A. Hoffman, J. R. Meyer, R. J. Wagner, F. J. Bartoli, M. A. Engelhardt, and H. Höchst, *Phys. Rev. B* **40**, 11693 (1989).
- [41] J. R. Chelikowsky and M. L. Cohen, *Phys. Rev. B* **14**, 556 (1976).
- [42] T. Brudevoll, D. S. Citrin, M. Cardona, and N. E. Christensen, *Phys. Rev. B* **48**, 8629 (1993).
- [43] A. A. Tonkikh, V. G. Talalaev, and P. Werner, *Semiconductors* **47**, 1452 (2013).
- [44] M. Jaros, *Phys. Rev. B* **37**, 7112 (1988).
- [45] S. Sant and A. Schenk, *IEEE Trans. Electron Devices* **3**, 164 (2015).
- [46] G. Sun, R. A. Soref, and H. H. Cheng, *Opt. Express* **18**, 19957 (2010).
- [47] Y.-H. Li, A. Walsh, S. Chen, W.-J. Yin, J.-H. Yang, J. Li, J. L. F. Da Silva, X. G. Gong, and S.-H. Wei, *Appl. Phys. Lett.* **94**, 212109 (2009).
- [48] J. Weber and M. I. Alonso, *Phys. Rev. B* **40**, 5683 (1989).
- [49] Y. Jiang, S. Huang, Z. Zhu, C. Zeng, Y. Fan, and Z. Jiang, *Nanoscale Res. Lett.* **11**, 102 (2016).
- [50] P. Guo, R. Cheng, W. Wang, Z. Zhang, J. Pan, E. S. Tok, and Y.-C. Yeo, *ECS J. Solid State Sci. Technol.* **3**, Q162 (2014).